Revealing crustal deformation and strain rate in Taiwan using InSAR and GNSS

Kathryn R. Franklin and Mong-Han Huang
Department of Geology, University of Maryland, College Park, MD, USA

Abstract

Interseismic deformation describes the gradual accumulation of crustal strain within the tectonic plate and along the plate boundaries before the sudden release as earthquakes. In this study, we use five years of high spatial and temporal geodetic measurements, including Global Navigation Satellite System (GNSS) and Interferometric Synthetic Aperture Radar (InSAR) to monitor 3-dimension interseismic crustal deformation and horizontal strain rate in Taiwan. We find significant deformation (strain rate > 8×10^{-6} yr^{-1}) along the plate boundary between the Philippine Sea Plate and the Eurasian plates in east Taiwan. The high strain rate in the southern part of the Western Foothills is distributed along a few major fault systems, which reveals the geometry of the deformation front in west Taiwan. Our results help identify active faults in southwest and north Taiwan that were not identified before. These findings can be insightful in informing future seismic hazard models.

Plain Language Summary

An earthquake cycle includes three phases: interseismic, coseismic, and postseismic. Interseismic deformation refers to the continuous crustal deformation that is built up by active tectonics. Depending on the relative motion between tectonic plates, the earthquake recurrence interval could vary by a few orders between different locations. As a result, knowing the crustal deformation rate and deformation accumulated in different fault zones can be useful for investigating future earthquake hazards. Using space geodesy tools like Global Navigation Satellite System (GNSS; commonly known as GPS) and Interferometric Synthetic Aperture Radar (InSAR), we can monitor surface deformation during the interseismic period. In this study, we monitor interseismic deformation in Taiwan using geodesy. We find that east Taiwan where two tectonic plates collide has the highest amount of deformation. In southwest and north Taiwan where most of the population resides, there is also high-level of deformation distributed across a few different faults, indicating that some of the faults have a higher risk generating future earthquakes. As a result, knowing the amount of faults slip and deformation built up during this interseismic period may inform us of potential future earthquake hazards.

Key Points

1. This study combines InSAR and GNSS and produces high-resolution 3-D interseismic crustal velocities and strain rate estimates in Taiwan.
2. Strain rate measurements show high surface strain cumulation along east and southwest Taiwan.
3. The surface strain rates and the earthquake hazard models based on seismology and field study-based are in good agreement.

1. Introduction

Taiwan is located between the Eurasian Plate and the Philippine Sea Plate. The Philippine Sea Plate moves towards northwest with a rate of > 80 mm/yr and causes an oblique collision with the Eurasian Plate. This collisional tectonics has given rise to a few geologic provinces, including (from west to east) Chianan Plain (CP), Western Foothills (WF), Hsueshan Range (HR), Central Range (CR), Longitudinal Valley (LV), and the Coastal Range (CoR) (**Figure 1a**). The high collision rate has resulted in a large number of earthquakes in Taiwan, and several devastating events have been located in west Taiwan where the majority of the population resides.

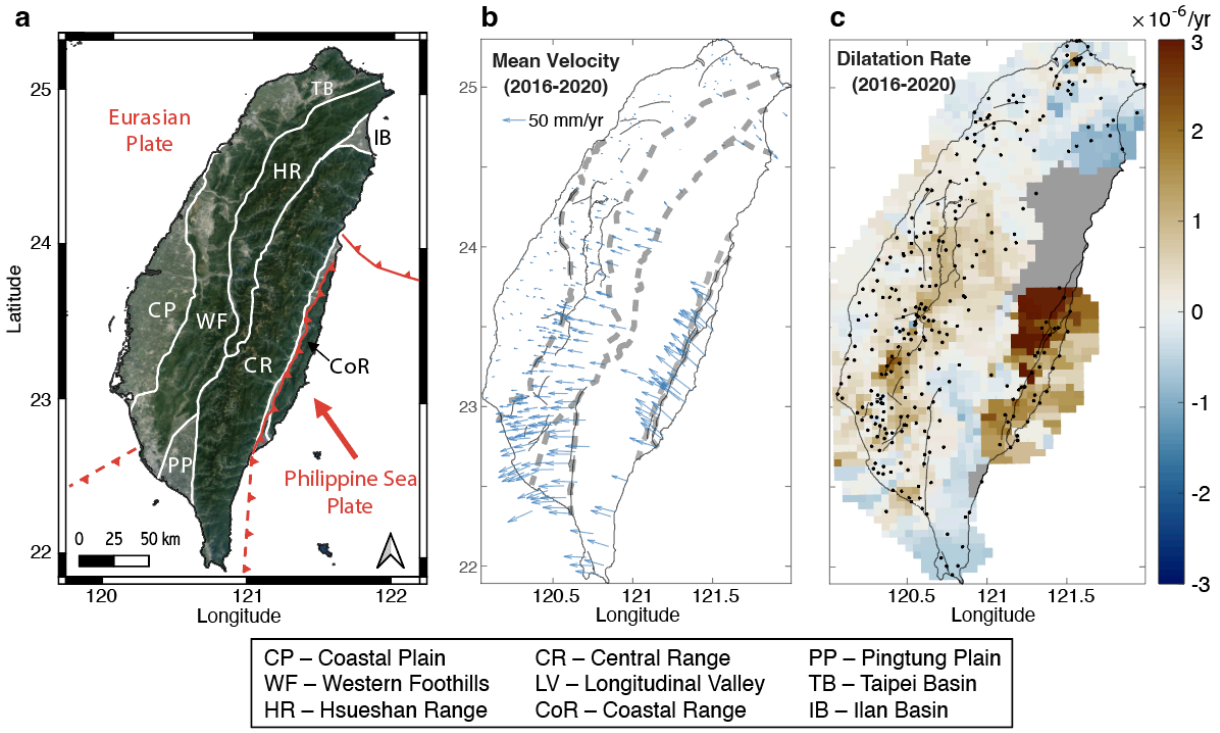

Figure 1. Tectonic setting and crustal deformation of Taiwan. (a) The solid and dashed red lines indicate plate boundaries. The white lines indicate geologic province boundaries. The full name of each geologic province and location is shown below the figure. (b) Mean interseismic GNSS velocities between 2016 and 2021. The black lines are active faults identified by CGS (2021). (c) Dilatation rate based on GNSS data in (b). Black dots are GNSS stations used for the analysis. Gray color represents areas without strain rate results due to lower GNSS network density. Red and blue represent contraction and extension rate (in 10^{-6} yr^{-1}), respectively.

Interseismic deformation describes the gradual accumulation of crustal strain within the tectonic plate and along the plate boundaries before its sudden release as earthquakes. Global Navigation Satellite Systems (GNSS) and Interferometric Synthetic Aperture Radar (InSAR) have been widely used to quantify the interseismic crustal deformation, and interseismic strain accumulation estimated from geodetic measurements can help evaluate potential seismic hazards (Avouac, 2015). Using campaign and continuous GNSS measurements, Yu et al. (1997) and Lin et al. (2010) observed > 80 mm/yr of convergent rate between east Taiwan and the Penghu Islands on the stable continental margin that is ~35 km west of Taiwan (white circles in **Figure 2c**). GNSS measurements also indicate a clockwise rotation in northeast Taiwan that

indicates a post-rift opening of the Okinawa Trough as well as lateral extrusion in southwest Taiwan (**Figure 1b**).

Although Taiwan has one of the highest GNSS network densities in the world, GNSS measurements alone still could not confidently identify interseismically creeping faults or deformation associated with closely spaced faults. For example, a GNSS-based dilatation rate map (**Figure 1c**) highlights regions undergoing interseismic contraction in east and southwest Taiwan and extension in northeast Taiwan in a broader scale, but it remains challenging to identify active faults or to determine interseismic fault locking depth of each fault system without high spatial resolution data. Alternatively, InSAR provides high spatial resolution measurements of surface deformation at a cm-level accuracy level (Bürgmann et al., 2000; Elliott et al., 2016). Recent work (e.g., Tong et al., 2012; Shen and Liu, 2020; Weiss et al., 2020) combines GNSS and InSAR to achieve a high spatial resolution with relatively high accuracy. This method is done by utilizing GNSS for the long-wavelength spatial deformation and InSAR for short-wavelength features. Huang and Evans (2019) estimated crustal deformation in southwest Taiwan using 6 years of InSAR-GNSS combined data and were able to characterize fault slip and locking depth of the major fault system using a total variation regularization approach for southwest Taiwan.

In this study, we employ ~5 years of GNSS and InSAR data to generate 3-D interseismic velocities in Taiwan based on data collected between 2016 and 2021. In application, we highlight surface deformation patterns using high resolution 3-D velocities and produce a horizontal strain rate analysis to identify interseismically active faults that can help produce better future seismic hazard models.

2. Data and Method

2.1 SAR and GNSS data collection

The SAR data was obtained from the European Space Agency's (ESA) Sentinel-1 mission for the Copernicus initiative. This mission collects C-band synthetic aperture radar (SAR) acquisitions with a wavelength of 56.7mm and provides single-look complex (SLC) products. In this study, we used Sentinel-1 SAR acquisitions from ascending track 69 and descending track 105 between November 2016 to July 2021. We do not include SAR data before November 2016 to avoid coseismic and to reduce early postseismic deformation of the 2016 M_W 6.4 MeiNong earthquake in southwest Taiwan (e.g. Huang, Tung, et al., 2016). However, our observation period includes the 2018 M_W 6.4 Hualien earthquake in northeast Taiwan (Huang and Huang, 2018). This is because there are sufficient amount of InSAR acquisitions before the Hualien earthquake and the epicenter is offshore. We estimate the coseismic and postseismic components of the Hualien earthquake from the time series analysis (**Supporting Information S1**).

The digital elevation models (DEM) were downloaded from NASA Jet Propulsion Lab's Shuttle Radar Topography Mission (SRTM) with 30m resolution and 3-arc second (Farr et al., 2007), which is stored in the USGS Measures project. The DEM data were used to remove elevation contributions to phase in InSAR images. The weather model used in the troposphere noise correction was downloaded from ECMWF (European Centre for Medium-Range Weather Forecasts) ERA5 weather model products.

The continuous GNSS time series data are processed and maintained by the Central Geologic Survey (CGS), the Central Weather Bureau, the Ministry of Interior, Taiwan, and the

GPS Laboratory at the Institute of Earth Science, Academia Sinica, Taiwan. This data is accessed from Academia Sinica, Taiwan. Additionally, each GNSS station time series was adjusted to remove network adjustment. Similar to the InSAR observation time period, we do not include the GNSS time series before November 2016 in order to reduce contribution from the 2016 MeiNong earthquake. As for the 2018 Hualien earthquake, we do not include GNSS stations within 50 km from the earthquake epicenter in the GNSS analysis.

2.2 InSAR time series processing

The InSAR products were processed using InSAR Scientific Computing Environment (ISCE) software developed at NASA JPL Caltech (Rosen et al., 2012). The TOPS Stack Processor is a module of the ISCE software package that enables SAR images to be combined to generate InSAR images (Fattahi et al., 2017), including applying phase unwrapping using Snaphu (Chen and Zebker, 2002). We used the Stack Sentinel module to generate SAR acquisition pairs by taking orbital data, DEM data, bounding box, auxiliary data (Sentinel-1 instrument parameters), the number of adjacent synthetic aperture radar (SAR) images to be processed and the start and end dates into account. Here we take a network of 3 of adjacent SAR acquisitions in the stack processing.

We used the *Miami InSAR Time Series Software in Python* (Mintpy) (Yunjun et al., 2019) to generate InSAR time series. Mintpy applies tropospheric noise corrections using the ECMWF weather model and generates the time series. We then estimate mean LOS velocities based on the ascending and descending InSAR time series. Mintpy uses a small baseline subsets approach to find the best fitting time series for the given interferograms while minimizing the implied

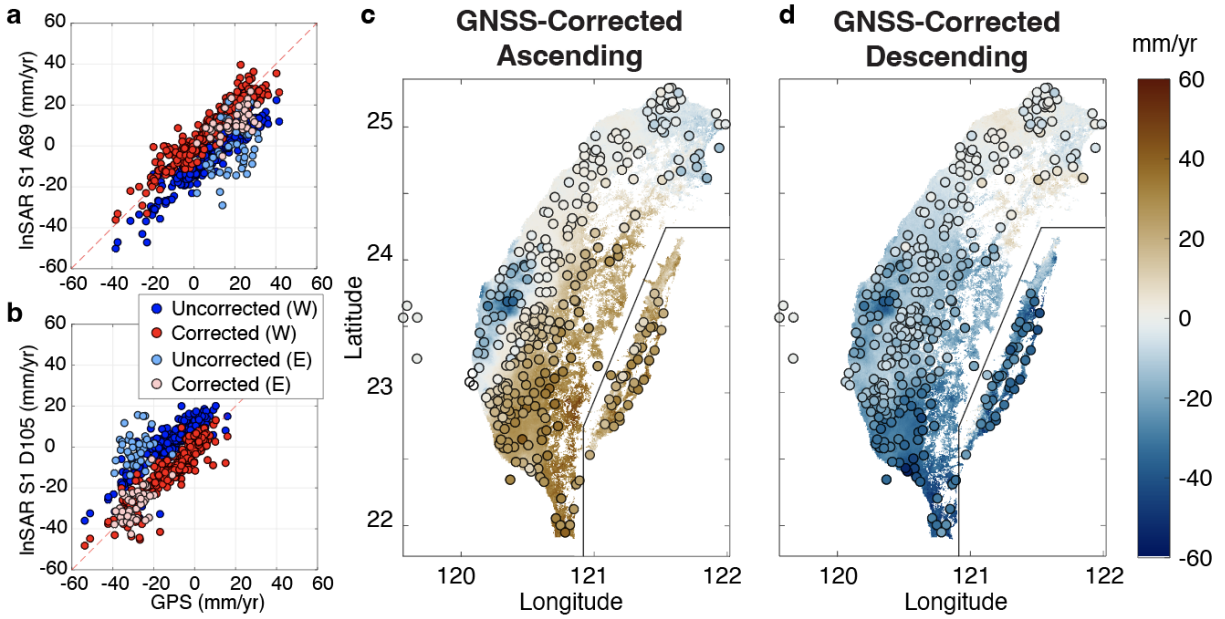

Figure 2. Comparison of InSAR and GNSS velocities. Comparison of velocities before and after correction for ascending (a) and descending (b) tracks. The red dash line in (a) and (b) represents a 1:1 ratio between GNSS and InSAR. W and E in (a) and (b) represent west and east Taiwan, respectively. Positive and negative values in (c) and (d) represent movement towards and award from the satellite LOS, respectively.

velocities (Bernardino et al., 2002). To avoid phase unwrapping errors due to steep mountain ranges and dense vegetation in the Central Range (CR in **Figure 1a**) that could generate a phase offset between west and east Taiwan, we separate the island into west and east Taiwan and perform phase unwrapping separately. Since each part has its own reference point, we merge InSAR results in east and west Taiwan onto a GNSS reference frame.

2.3 Generation of 3-D velocities

Here we briefly document the process of retrieving mean velocities from InSAR and GNSS time series. Details regarding merging InSAR datasets between west and east Taiwan and performing a joint inversion of InSAR and GNSS to estimate 3-D velocities can be found in **Supplementary Information S1**. This process estimates mean velocities from the ascending and descending LOS time series using a polynomial function fit for each InSAR pixel and GNSS station (**Figure S1** as an example). To adjust InSAR velocities to the GNSS reference frame, we first calculate GNSS velocities in InSAR ascending and descending LOS from the 3 components (east-west, north-south, and vertical). For each GNSS station, we use InSAR pixels within 500 m distance from the GNSS station to estimate the average InSAR velocity at the GNSS station in order to reduce InSAR phase noise. As shown in **Figure 2a,b**, besides a consistent shift between InSAR and GNSS ascending or descending velocities, InSAR and GNSS results are quite consistent. This is shown by the nearly 1:1 ratio plus an offset between InSAR and GNSS data distribution (blue circles in **Figure 2c**) due to different reference points between GNSS and InSAR. We use a least square approach to fit InSAR into GNSS-simulated LOS (red circles in **Figure 2c**). After this adjustment, we interpolate GNSS velocities to InSAR samplings using *cubic* interpolation in Matlab. Once this is done, we use the equations that relate LOS and 3-D components for both InSAR and GNSS, and calculate 3-D velocity of each InSAR pixel through a least square inversion. We also use the estimated GNSS and InSAR uncertainty as a weighting matrix in the inversion.

3. 3-D interseismic velocities

The 3-D surface deformation results are shown in **Figure 3**, and the associated uncertainties are shown in **Figures S2 and S3**. The uncertainty analysis, including data misfit estimate and InSAR noise structure is described in **Supporting Information S2**. We consider the mean velocity results to be representative of the interseismic crustal velocities in Taiwan since we have removed contribution from major earthquakes (**Section 2.1**). In the horizontal components, the north-south motion is smoother because it is mostly constrained by the interpolated GNSS data, since InSAR has lower sensitivity to north-south motions. There are no estimated velocities along the east side of the Central Range (CR in **Figure 1a**) because of the high topographic relief that decreases the coherence in most interferograms. The 3-D velocities show up to 40 mm/yr southwestward motion in southwest Taiwan. In east Taiwan, there is > 40 mm/yr northwestward motion along the Longitudinal Valley Fault (LVF in **Figure 3b**). There is observable surface subsidence in the north Coastal Range (CoR in **Figure 1a**), whereas there is more than 20 mm/yr of uplift in the south CoR, which is similar to finding by Hsu and Bürgmann (2006). Along the Central Range, there is up to 20 mm/yr uplift. In the Chianan Plain (CP in **Figure 1a**), there is more than 40 mm/yr surface subsidence due to anthropogenic groundwater pumping (Hung et al., 2010, 2011; Tung and Hu, 2012; Huang, Bürgmann et al., 2016). We plot three

transects across the major geologic structure of Taiwan to highlight significant deformation across the island.

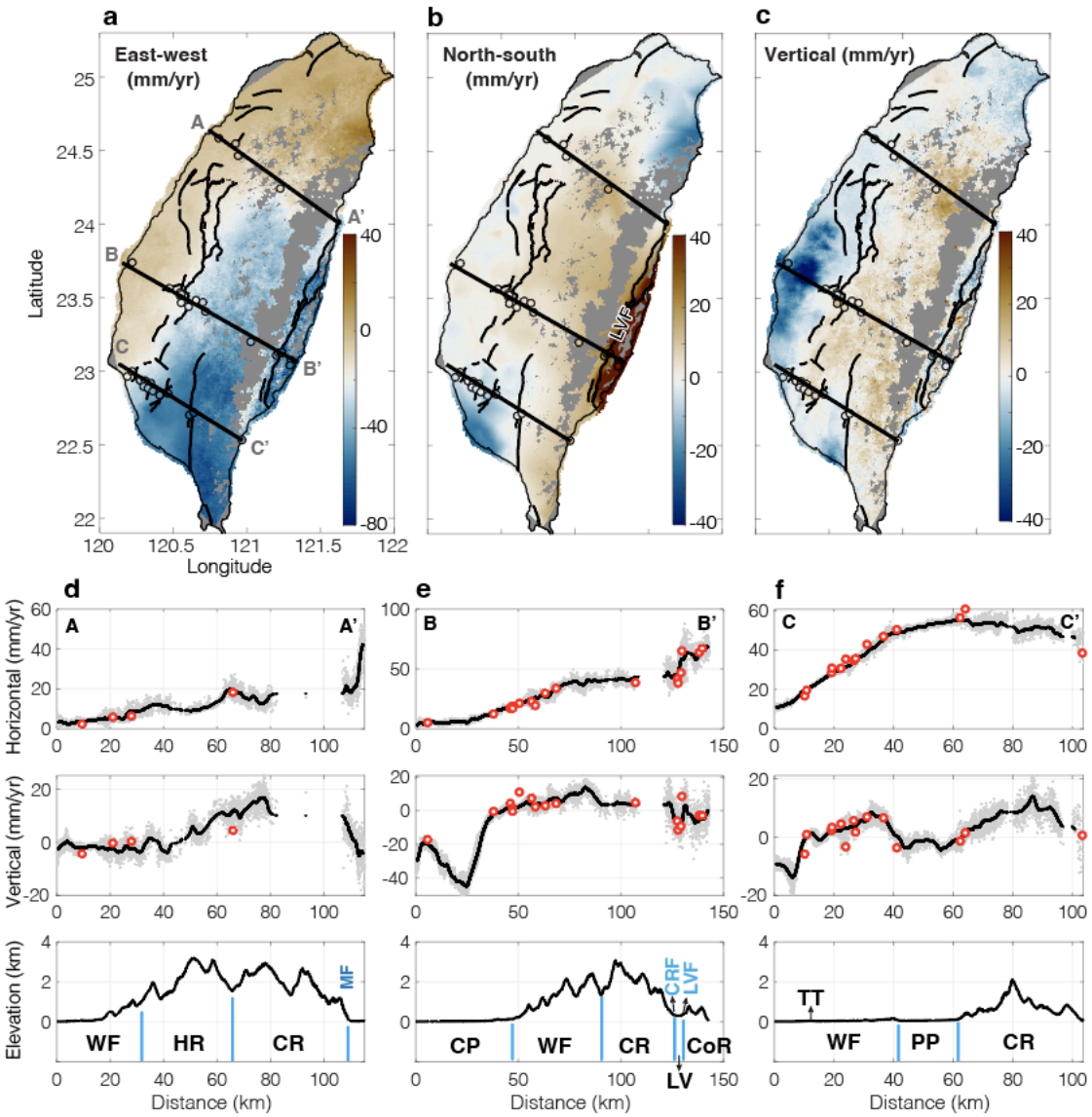

Figure 3. 3-D velocities based on the InSAR-GNSS combined dataset. (a) East-West, (b) North-South, and (c) Vertical velocities. Positive values represent eastward, northward, or upward motions. The black lines are active faults identified by CGS (2021). The colored circles are GNSS stations plotted in the transects. (d), (e), and (f) are three selected transects across the island. In each subplot, the top and middle rows are the horizontal (square root of the east-west and north-south components) and vertical components, respectively. The gray dots are InSAR horizontal or vertical velocities, with the black lines representing the smoothed velocities (smoothing widow size is 100 pixels). The red circles are GNSS mean velocity along the same transect. The bottom of each subplot shows surface topography. The vertical blue lines indicate the geologic boundaries. TT is the location of the Tainan Tableland, and the other abbreviations are the same as those in **Figure 1**.

In transect A (**Figure 3d**), the increase of horizontal motion is not linear, implying change of fault slip rate or locking depth in different geologic units. There is an up to 20 mm/yr increase

of horizontal motion across the Milun Fault (MF in **Figure 3d**). However, this motion could be associated with the 2018 Hualien earthquake that significant slip along the Milun Fault (Huang and Huang, 2018), and the postseismic contribution in the InSAR time series may not be entirely removed. The vertical motion is relatively stable in the Western Foothills (WF), followed by a total of 17 mm/yr of uplift in the Hsueshan Range (HR).

Transect B (**Figure 3e**) goes across CP, Western Foothills (WF), CR, and CoR. The horizontal velocity increases by 40 mm/yr from CP to west CR, followed by another rapid increase (20 mm/yr) across LVF. In the vertical component, there is > 40 mm/yr of surface subsidence likely due to anthropogenic activities. The uplift rate gradually increases from WF to CR with a peak uplift rate ~15 mm/yr, which is similar to the long-term uplift rate in Taiwan based on exhumation rate measurements of rocks (Ching et al., 2011). There is ~10 mm/yr of subsidence in the Longitudinal Valley (LV) between CR and CoR. The clear horizontal and vertical velocity offset along LVF suggest shallow fault creep (Lee et al., 2005; Champenois et al., 2012). Although there is a clear vertical offset along the CRF, a lack of horizontal offset across CRF implies the subsidence in LV here could be due to anthropogenic activity. The location of transect B is similar to that presented in both Ching et al. (2011) and Hsu et al. (2018). While the horizontal component is similar to that in Ching et al. (2011), the vertical component is more similar to Hsu et al. (2018).

Transect C (**Figure 3d**) goes across the most active structure of WF. There is ~50 mm/yr of increase in horizontal velocity from west to east WF. The velocity starts to decrease by ~3 cm/yr from west to east CR. In the vertical component, there is subsidence west of the Tainan Tableland (TT in **Figure 3f**), likely related to anthropogenic groundwater pumping. We find clear uplift in WF and CR, but close to no vertical motion in the Pingtung Plain (PP in **Figure 1a**).

4. Strain rate analysis

We calculate the strain rate tensor of Taiwan from the InSAR-GNSS combined dataset. Since surface displacements associated with major earthquakes were removed or estimated in the time series, we consider this dataset representing the interseismic deformation of Taiwan. To reduce computation time, we first downsample the horizontal velocities to 500 m pixel spacing. Since strain rate is differential velocities of pixels divided by pixel distance, it could dramatically amplify short-wavelength noise in InSAR and make the result uninterpretable. For example, 1 mm of noise in 1-D velocity between two pixels 500 m apart can cause longitudinal strain equivalent to 2×10^{-6}. We therefore consider using a group of pixels within a characteristic distance for constructing the strain rate tensor of each grid point. To explore the appropriate length scale of the smoothing, we use a semi-variogram approach suggested by Sudhaus and Jónsson (2009) in a region that is stable in west Taiwan (**Supplementary Information S3)**. We estimate spatially correlated signals in the horizontal velocities and find a characteristic distance of ~7 km (**Figure S6**). Based on this value, when we generate the strain rate tensors we take into account velocities of 144 nearby pixels of each grid point. This number is obtained from the number of pixels that occupy a circular area with 3.4 km radius and 500 m pixel spacing.

The dilatation and the second invariant of the strain rate with 1 km grid spacing are shown in **Figure 4**. In order to reduce the complexity of the fault naming system, we use fault ID numbers consistent with Central Geologic Survey in Taiwan (CGS, 2021) and use the fault ID number than fault names for most of the time hereafter. The fault names are listed below **Figure 4f**. The dilatation rate from the InSAR-GNSS dataset (**Figure 4a**) has much higher spatial resolution than

217 the GNSS-only results (**Figure 1c**). In east Taiwan, the dilatation rate shows a very localized
218 deformation along LVF. In west Taiwan, we find higher contraction rate within WF, along

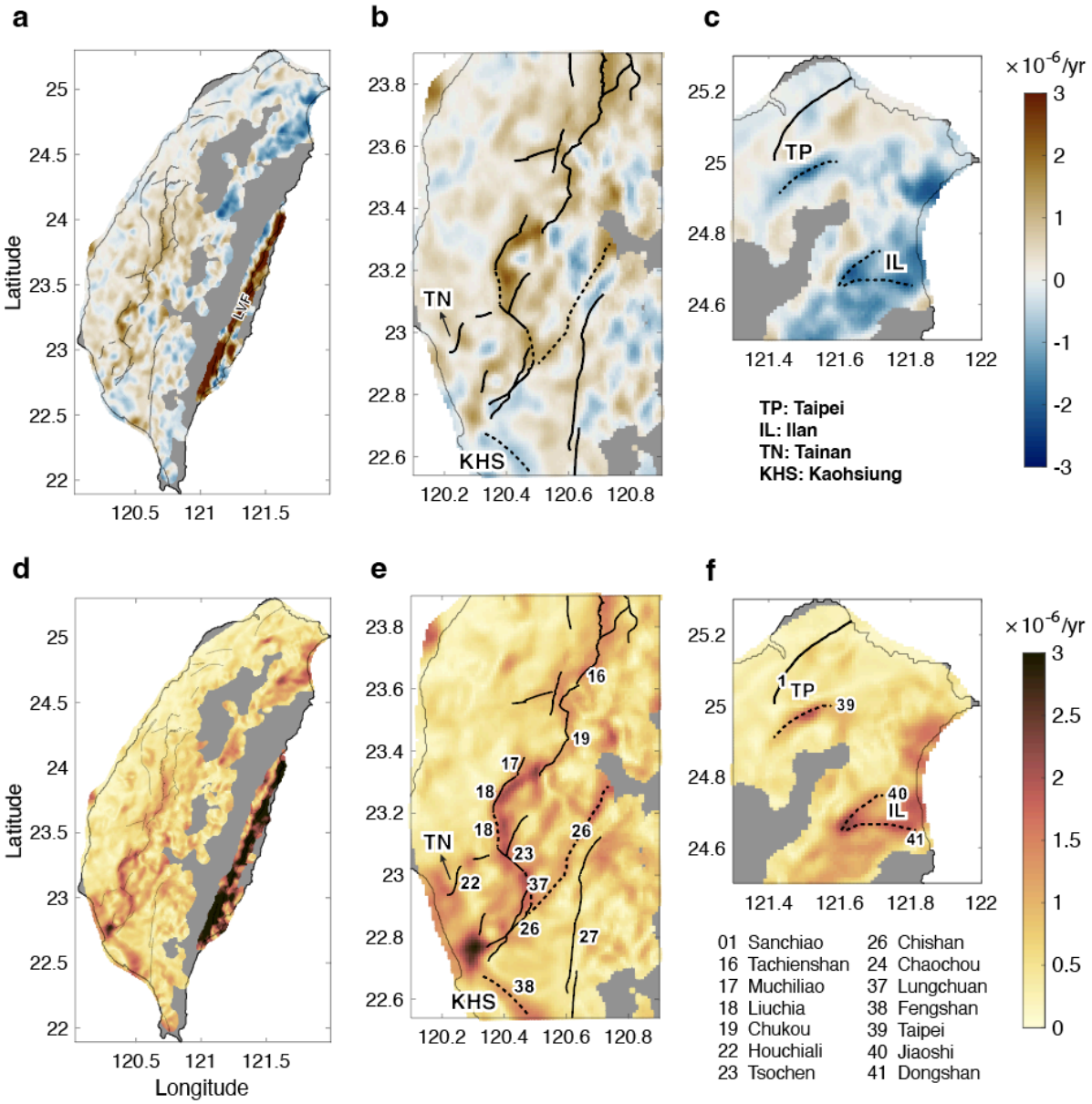

Figure 4. InSAR-GNSS combined strain rate in Taiwan. (a) Dilatation rate. Warm and cold colors indicate contraction and extension, respectively. The color scale is shown in (c). (b) and (c) show the dilatation rate in southwest and north Taiwan, respectively. (d) Second invariant of the strain rate tensor. Warmer color indicates greater amount of deformation. The color scale is shown in (f). (e) and (f) show the second invariant in southwest and north Taiwan, respectively. The black lines in each plot are the active fault traces identified by CGS (2021). In (b) and (c), TN, KHS, TP, and IL are cities (names listed below c). The dashed lines in (b), (c), (e), and (f) are potentially active faults based on strain rate analysis. The numbers in (e) and (f) are faults with names listed below (f). Naming of F37-41 is based on Chen (2016).

several major faults (black fault lines in **Figure 4b**). The distribution of the high second invariant may reveal the deformation front of west Taiwan. In north Taiwan (**Figure 4c**), there is a clear extension along the geologic boundary between CR and HR. We also find a localized extension in the south side of Taipei (TP in **Figure 4c**).

The second invariant of the strain rate tensor (**Figure 4d**) shows the total amount of strain rate (both dilatation and shear). Similar to the dilatation rate, the highest deformation is along LVF with rate > 8×10^{-6} yr^{-1}. Southwest Taiwan has the next highest strain rate after LVF. In a detailed view (**Figure 4e**), there is increased deformation along the major faults (labeled in numbers in **Figure 4e**). This result provides much better spatial resolution of deformation than the GNSS-only products (**Figure 1c**). We additionally find higher strain rate along faults that were not considered active by CGS (2021) but were identified by Chen (2016) based on fieldwork and paleoseismology (indicated by the dashed lines in **Figure 4b,c,e,f)**. In northern Taiwan, in addition to fault ID 39 (or F39), we also find higher deformation in the north and south sides of IL (F40 and F41).

5. Comparing with seismic hazard models

Chan et al. (2020) provided the 2020 version of the Taiwan Earthquake Model (TEM) of Probabilistic Seismic Hazard Analysis (PSHA) following an initial model built by Wang et al. (2016) and fault information by Shyu et al. (2016, 2020). The TEM PSHA model estimates seismic hazard based on a seismogenic structure database, an updated earthquake catalog, time-dependent rupture model, and a revised area source model to estimate the seismic hazard map of Taiwan. With incorporation of Vs30 (shear-wave velocity in the top 30 m depth) for calculating site amplification, the TEM PSHA model identified a few fault structures with an increased seismic hazard potential close to the IB, LV, and southwest WF (see **Figure 1a** for locations). In this section we compare the TEM PSHA model (called *seismic hazard model* hereafter) that predicts future earthquake probability, with the second invariant of the strain rate tensor, which highlights surface strain accumulation over time. Although they do not need to agree, regions with higher interseismic strain accumulation tend to be more seismically active.

We find some similarity between the seismic hazard model and the second invariant of the strain rate tensor. In southwest Taiwan where interseismic strain rate is higher (**Figure 4e**), both F17 and F18 have high seismic potential in the seismic hazard model. However, the distribution of high seismic potential south of F18 is different, where high strain rate diverts into F37 and F22. F22 is in east Tainan Tableland with an estimated ~10 mm/yr creep rate from previous studies (e.g., Huang et al., 2006; Le Béon et al., 2019), but here we additionally find surface deformation west of TN. Further to the southwest side of F26 and along F38, the seismic hazard map does not predict a particularly high seismic probability, whereas high interseismic strain rate is observed. The high strain rate between F22, F26, and F38 could be of concern because Tainan (TN) and Kaohsiung (KHS), the two major cities, are located nearby the fault structures.

In north Taiwan, both the second invariant (**Figure 4f**) and the seismic hazard model show higher deformation and higher seismic probability in Ilan (IL). In Taipei (TP), the capital city of Taiwan, we observed extension strain rate of ~2×10^{-6} yr^{-1} along F39, while the seismic hazard model does not predict a higher hazard potential. F39 (Taipei Fault) has been identified as an inactive reverse fault, but earthquake focal mechanisms near this region show a sign of extension

(Teng et al., 2001). There is also a clear surface subsidence in the TP (**Figure 3c**) as a result of groundwater pumping which is inducing soil compaction, aquifer deformation, and general subsidence (Chen et al., 2007). We cannot discern whether fault creep could have contributed to the surface subsidence near F39. Future studies on seasonal variation of surface movement and how it relates to precipitation and groundwater discharge data may provide further insight into identifying the cause of surface subsidence in this time period.

Again, interseismic surface strain rates do not have to agree with seismic hazard models because they do not inform coseismic displacement. However, a better knowledge of interseismic fault slip, fault locking depth, and detection of active faults may provide significant contributions in advancing fault geometry and slip models for the seismic hazard models. For example, the second invariant result identifies additional faults that are currently active but are not identified as active faults possibly due to limited field mapping or a lack of seismicity during aseismic fault creep, hence not detected using seismology. Future interseismic fault slip models with geodetic constraints can further incorporate fault slip budget (Avouac, 2015). Probabilistic earthquake likelihood models using both geodetic measurements and seismic catalog (e.g., Rollins and Avouac, 2019) may provide insightful contribution to future seismic hazard models.

6. Conclusions

Combining the capabilities of GNSS and InSAR, we can better reveal interseismic crustal deformation of Taiwan. Through a series of GNSS and InSAR comparisons, we find consistency between the two datasets. The InSAR-GNSS combined result shows greater deformation in east and southwest Taiwan, and there is > 40 mm/yr of surface subsidence in west Taiwan due to anthropogenic water pumping and up to 20 mm/yr of uplift in the Central Range. Strain rate analysis suggests > 8×10^{-6} yr^{-1} surface contraction rate along the Longitudinal Valley Fault, and there is also a higher level of contraction in the southwest Western Foothills. The high-resolution strain rate results may reveal the distribution of the deformation front of Taiwan. Our work demonstrates a high spatial resolution of surface deformation that can be revealed by publicly available SAR data with open-source processing tools. Our results highlight creeping faults in east and southwest Taiwan and help identify active faults that were not identified before. These findings can be useful for informing future seismic hazard models.

Acknowledgements

We want to thank Eileen Evans, Chung Huang, Vedran Lekić, and Laurent Montesi for their insightful comments on the original manuscript. MH thanks Kathrine Udell Lopez for proofreading the manuscript. We also thank the GPS laboratory at the Academia Sinica in Taiwan who actively maintains the GNSS stations. This work is supported by NSF EAR 2026099.

Data Sources and Availability Statement

The SLC products containing the SAR images were downloaded from the Alaska Satellite Facility (ASF), University of Alaska database. The precise orbital data of the Sentinel-1 satellites were downloaded from ESA Science Hub. The stack process is part of the ISCE InSAR processing software package (Rosen et al., 2012). Mintpy is an open-source InSAR time series processing software (Yunjin et al., 2019). The InSAR-GNSS dataset and the strain rate results can be found in the Supplementary Datasets. It will also be archived in Zenodo after the peer review process.

References

Avouac, J.-P. (2015). From geodetic imaging of seismic and aseismic fault slip to dynamic modeling of the seismic cycle. Annual Review of Earth and Planetary Sciences, 43(1), 233–271. https://doi.org/10.1146/annurev-earth-060614-105302

Bernardino, P., Fornaro, G., Lanari, R., and Sansosti, E. (2002), Monitoring based on small baseline differential SAR interferograms, *IEEE Transactions on Geoscience and Remote Sensing*, 40, 2375-2383.

Bürgmann, R., Rosen, P. A., & Fielding, E. J. (2000). Synthetic Aperture Radar Interferometry to Measure Earth's Surface Topography and Its Deformation. *Annual Review of Earth and Planetary Sciences, 28*(1), 169-209. doi:10.1146/annurev.earth.28.1.169.

Central Geological Survey (CGS), MOEA (2021). Active fault map of Taiwan. Retrieved from https://faultnew.moeacgs.gov.tw/ckfinder/connector?command=Proxy&type=Attach&currentFolder=/&fileName=2021%20Taiwan%20Fault%20Distribution%20Map%28English%20Version%29.jpg&c=2&p=tblAbout_1&l=4

Champenois, J., Fruneau, B., Pathier, E., Deffontaines, B., Lin, K.-C., and Hu, J.-C. (2012). Monitoring of active tectonic deformations in the Longitudinal Valley (Eastern Taiwan) using Persistent Scatterer InSAR method with ALOS PALSAR data. *Earth and Planetary Science Letters*, *337-338*, 144-155. http://dx.doi.org/10.1016/j.epsl.2012.05.025

Chan, C.-H., Ma, K.-F., Shyu, J. B. H., Lee, Y.-T., Wang, Y.-J., Gao, J.-C., Yen, Y.- T., & Rau, R.-J. (2020). Probabilistic seismic hazard assessment for Taiwan: TEM PSHA2020. *Earthquake Spectra, 36*, 137–159. https://doi.org/10.1177/8755293020951587

Chen, C. W., & Zebker, H. A. (2002). Phase unwrapping for large SAR interferograms: Statistical segmentation and Generalized Network Models. *IEEE Transactions on Geoscience and Remote Sensing*, *40*(8), 1709–1719. https://doi.org/10.1109/tgrs.2002.802453

Chen, C.-T., Hu, J.-C., Lu, C.-Y., Lee, J.-C., & Chan, Y.-C. (2007). Thirty-year land elevation change from subsidence to uplift following the termination of groundwater pumping and its geological implications in the metropolitan taipei basin, Northern Taiwan. *Engineering Geology*, *95*(1-2), 30–47. https://doi.org/10.1016/j.enggeo.2007.09.001

Chen, W.-S. (2016), Introduction to Taiwan geology (in Chinese), published by *Geological Society Located in Taipei*. 250 pp.

Ching, K.-E., Hsieh, M.-L., Johnson, K. M., Chen, K.-H., Rau, R.-J., and Yang, M. (2011), Modern vertical deformation rates and mountain building in Taiwan from precise leveling and continuous GPS observations, 2000–2008, *J. Geophys. Res.*, 116, B08406, doi:10.1029/2011JB008242.

Elliott, J. R., Walters, R. J., and Wright, T. J., (2016), The role of space-based observation in understanding and responding to active tectonics and earthquakes, *Nat. Commun.*, *7*, 13844, doi:10.1038/ncomms13844.

Farr, T. G., et al. (2007), The shuttle radar topography mission, Rev. Geophys., 45, RG2004, doi:10.1029/2005RG000183.

Fattahi, H., Agram, P., & Simons, M. (2017). A Network-Based Enhanced Spectral Diversity Approach for TOPS Time-Series Analysis. *IEEE Transactions on Geoscience and Remote Sensing, 55*(2)*,* 777-786. doi:10.1109/tgrs.2016.2614925

Hsu, L., and Bürgmann, R. (2006), Surface creep along the Longitudinal Valley fault, Taiwan from InSAR measurements, *Geophys. Res. Lett.*, 33, L06312, doi:10.1029/2005GL024624.

Hsu, Y.-J., Lai, Y.-R., You, R.-J., Chen, H.-Y., Teng, L. S., Tsai, Y.-C., et al. (2018). Detecting rock uplift across southern Taiwan mountain belt by integrated GPS and leveling data. *Tectonophysics*, *744*, 275–284. https://doi.org/10.1016/j.tecto.2018.07.012

Huang, M.-H., Hu, J.-C., Hsieh, C.-S., Ching, K.-E., Rau, R.-J., Pathier, E., et al. (2006). A growing structure near the deformation front in SW Taiwan as deduced from SAR interferometry and geodetic observation. *Geophysical Research Letters*, *33*, L12305. https://doi.org/ 10.1029/2005GL025613

Huang, M.-H., Bürgmann, R., & Hu, J.-C. (2016). Fifteen years of surface deformation in southwestern Taiwan: Insight from SAR inter- ferometry. *Tectonophysics*, *692*, 252–264. https://doi.org/10.1016/j.tecto.2016.02.021

Huang, M.-H., Tung, H., Fielding, E. J., Huang, H.-H., Liang, C., Huang, C., & Hu, J.-C. (2016). Multiple fault slip triggered above the 2016 *Mw* 6.4 MeiNong earthquake in Taiwan. *Geophysical Research Letters*, *43*, 7459–7467. https://doi.org/10.1002/2016GL069351

Huang, M.-H., & Huang, H.-H. (2018). The complexity of the 2018 M_w 6.4 Hualien earthquake in east Taiwan. *Geophysical Research Letters*, 45, 13,249– 13,257. https://doi.org/10.1029/2018GL080821

Huang, M.-H., & Evans, E. L. (2019). Total variation regularization of geodetically constrained block models in Southwest Taiwan. *Journal of Geophysical Research: Solid Earth*, *124*. https://doi.org/10.1029/2019JB018076

Hung, W.-C., Hwang, C., Chang, C.-P., Yen, J.-Y., Liu, C.-H., & Yang, W.-H., 2010. Monitoring severe aquifer-system compaction and land subsidence in Taiwan using multiple sensors: Yunlin, the southern Choshui River Alluvial Fan. Environ. Earth Sci. 59, 1535–1548.

Hung, W.-C., Hwang, C., Chen, Y.-A., Chang, C.-P., Yen, J.-Y., Hooper, A., & Yang, C.-Y., 2011. Surface deformation from persistent scatterers SAR interferometry and fusion with leveling data: a case study over the Choushui River Alluvial Fan, Taiwan. Remote Sens. Environ. 115, 957–967.

Le Béon, M., Marc, O., Suppe, J., Huang, M.-H., Huang, S.-T., & Chen, W.-S. (2019). Structure and deformation history of the rapidly growing Tainan anticline at the deformation front of the Taiwan mountain belt. *Tectonics*, 38, 3311– 3334. https://doi.org/10.1029/2019TC005510

Lee, J.-C., Angelier, J., Chu, H.-T., Hu, J.-C., Jeng, F.-S., (2005). Monitoring active fault creep as a tool in seismic hazard mitigation. Insights from creepmeter study at Chihshang, Taiwan. C. R. Geosci. 337 (13), 1200–1207.

Lin, K.-C., Hu, J.-C., Ching, K.-E., Angelier, J., Rau, R.-J., Yu, S.-B., et al. (2010). GPS crustal deformation, strain rate, and seismic activity after the 1999 chi-chi earthquake in Taiwan. *Journal of Geophysical Research*, *115*(B7), B07404. https://doi.org/10.1029/2009JB006417

Rollins, C., & Avouac, J.-P. (2019). A geodesy- and seismicity-based local earthquake likelihood model for central Los Angeles. *Geophysical Research Letters*, 46, 3153– 3162. https://doi.org/10.1029/2018GL080868

Rosen, P. A., Gurrola, E., Sacco, G. F., & Zebker, H. (2012), The InSAR scientific computing environment, Proc. EUSAR, Nuremberg, Germany, 730–733.

Shen, Z.-K., & Liu, Z. (2020). Integration of GPS and InSAR data for resolving 3-dimensional crustal deformation. *Earth and Space Science*, 7, e2019EA001036. https://doi.org/10.1029/2019EA001036

Shyu, J. B. H., Chuang, Y. R., Chen, Y. L., Lee, Y. R., & Cheng, C. T. (2016). A New On-Land Seismogenic Structure Source Database from the Taiwan Earthquake Model (TEM) Project for Seismic Hazard Analysis of Taiwan. *Terrestrial, Atmospheric & Oceanic Sciences*, *27*(3).

Shyu, J. B., Yin, Y.-H., Chen, C.-H., Chuang, Y.-I., & Liu, S.-Ch. (2020). Updates to the on-land seismogenic structure source database by the Taiwan Earthquake Model (TEM) project for seismic hazard analysis of Taiwan. *Terrestrial Atmospheric and Oceanic Sciences. 31,* 469-478. 10.3319/TAO.2020.06.08.01.

Sudhaus, H., & Jónsson, S. (2009). Improved source modelling through combined use of Insar and GPS under consideration of correlated data errors: Application to the June 2000 Kleifarvatn earthquake, Iceland. *Geophysical Journal International*, *176*(2), 389–404. https://doi.org/10.1111/j.1365-246x.2008.03989.x

Teng, L. S., Lee, C.-T., Peng, C.-H., Chu, J.-J., and Chen, W.-F. (2001). Origin and geological evolution of the Taipei Basin, northern Taiwan. West. Pac. Earth Sci.s 1, 115-142

Tong, X., Sandwell, D. T., & Smith-Konter, B. (2013). High-resolution interseismic velocity data along the San Andreas Fault from GPS and InSAR. *Journal of Geophysical Research: Solid Earth, 118*(1), 369-389. doi:10.1029/2012jb009442

Tung, H., Hu, J.-C., 2012. Assessments of serious anthropogenic land subsidence in Yunlin County of central Taiwan from 1996 to 1999 by persistent scatterers InSAR. Tectonophysics 578, 126–135.

Wang, Y.-J., Chan, C.-H., Lee, Y.-T., Ma, K.-F., Shyu, J. B. H., Rau, R.-J., & Cheng, C.-T. (2016). Probabilistic seismic hazard assessment for Taiwan. Terrestrial, Atmospheric and Oceanic Sciences, 27(3), 325-. doi:10.3319/TAO.2016.05.03.01(TEM)

Weiss, J. R., Walters, R. J., Morishita, Y., Wright, T. J., Lazecky, M., Wang, H., . . . Parsons, B. (2020). High-Resolution Surface Velocities and Strain for Anatolia from Sentinel-1 InSAR and GNSS Data. *Geophysical Research Letters, 47*(17). doi:10.1029/2020gl087376

Yu, S.-B., Chen, H.-Y., & Kuo, L.-C. (1997). Velocity field of GPS stations in the Taiwan area. *Tectonophysics*, *274*(1- 3), 41–59. https://doi.org/10.1016/S0040-1951(96)00297-1

Yunjun, Z., Fattahi, H., & Amelung, F. (2019). Small baseline InSAR time series analysis: Unwrapping error correction and noise reduction. *Computers and Geosciences*, 133, 104331. https://doi.org/10.1016/j.cageo.2019.104331

References From the Supporting Information

Fagereng, Å., & Biggs, J. (2019). New perspectives on 'geological strain rates' calculated from both naturally deformed and actively deforming rocks. Journal of Structural Geology, 125, 100-110. https://doi.org/10.1016/j.jsg.2018.10.004

Hussain, E., Hooper, A., Wright, T. J., Walters, R. J., & Bekaert, D. P. (2016). Interseismic strain accumulation across the central North Anatolian Fault from iteratively unwrapped InSAR measurements. *Journal of Geophysical Research: Solid Earth, 121(*12). https://doi.org/10.1002/2016JB013108

Pagani, C., Bodin, T., Métois, M., & Lasserre, C. (2021). Bayesian Estimation of Surface Strain Rates From Global Navigation Satellite System Measurements: Application to the Southwestern United States. Journal of Geophysical Research: Solid Earth, 126(6). doi:10.1029/2021jb021905

Watson, A. R., Elliott, J. R., & Walters, R. J. (2022). Interseismic strain accumulation across the main recent fault, SW Iran, from Sentinel-1 Insar Observations. *Journal of Geophysical Research: Solid Earth*, *127*(2). https://doi.org/10.1029/2021jb022674